JACS
JOURNAL OF THE AMERICAN CHEMICAL SOCIETY
Article
Cite This: J. Am. Chem. Soc. XXXX, XXX, XXX−XXX
pubs.acs.org/JACS

# Layered Halide Double Perovskites: Dimensional Reduction of $Cs_2AgBiBr_6$

Bridget A. Connor,[†] Linn Leppert,[‡] Matthew D. Smith,[†] Jeffrey B. Neaton,*[,§,#,∥] and Hemamala I. Karunadasa*[,†]

[†]Department of Chemistry, Stanford University, Stanford, California 94305, United States
[‡]Institute of Physics, University of Bayreuth, 95440 Bayreuth, Germany
[§]Molecular Foundry, Lawrence Berkeley National Laboratory, Berkeley, California 94720, United States
[#]Department of Physics, University of California Berkeley, Berkeley, California 94720, United States
[∥]Kavli Energy NanoScience Institute at Berkeley, Berkeley, California 94720, United States

Supporting Information

**ABSTRACT:** We investigate the consequences of dimensional confinement on halide double perovskites by synthesizing two-dimensional analogues of the recently reported three-dimensional double perovskite $Cs_2AgBiBr_6$. The layered perovskites $(BA)_4AgBiBr_8$ (**1**) and $(BA)_2CsAgBiBr_7$ (**2**) (BA = $CH_3(CH_2)_3NH_3^+$) feature metal-halide sheets of mono and bilayer thickness, respectively, where the ordered double-perovskite lattice is partitioned by organic cations. Electronic structure calculations indicate that the indirect bandgap of $Cs_2AgBiBr_6$ becomes direct when the infinitely thick inorganic lattice is reduced to monolayer thickness. Calculations on model systems allow us to separate the effects of dimensional reduction from those of the accompanying structural distortions in the inorganic sublattice. Detailed optical characterization shows that the photophysical properties of **1** and **2** are markedly different than those of their well-studied lead-halide analogs. Hybrid layered derivatives of double perovskites substantially expand on the substitutional flexibility of halide perovskites to encompass greater compositional and electronic diversity.

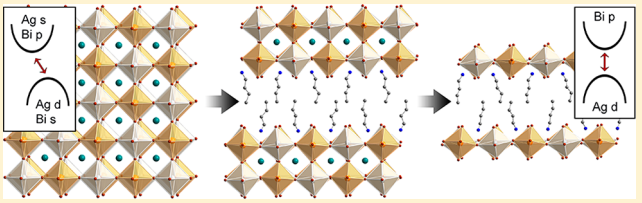


## INTRODUCTION

Dimensional reduction, or conversion of a structure to a lower-dimensional derivative,[1] affords dramatic changes in a material's physical and electronic properties. For example, upon chemical or physical exfoliation of the bulk material to a single monolayer, transition metal dichalcogenides such as $MoS_2$ exhibit a transition from an indirect to a direct bandgap.[2] Similarly, dimensional reduction of the inorganic sublattice in organic−inorganic hybrids produces the effects of electronic confinement, but in bulk solids without nanostructuring. These effects are well demonstrated by lead-halide perovskites.[3] The three-dimensional (3D) lead-iodide perovskites have small bandgaps, disperse bands, and weak exciton (excited electron−hole pair) binding energies beneficial for solar-cell absorbers.[4] Typical two-dimensional (2D) lead-halide perovskites, in contrast, exhibit larger bandgaps, less disperse bands, and exceptionally high exciton binding energies, which yield diverse luminescence behavior that has been exploited in light-emitting-diode[5] and phosphor[6] applications. Although hundreds of 2D hybrid perovskites have been reported, most are based on a limited number of divalent cations such as $Pb^{2+}$, $Cu^{2+}$, $Mn^{2+}$, $Cr^{2+}$, $Sn^{2+}$, and $Cd^{2+}$,[3a] although trivalent $Bi^{3+}$ and $Sb^{3+}$ have been incorporated through the inclusion of lattice vacancies.[7] Double perovskites, containing an ordered arrangement of two different metal cations, can accommodate more diverse metals and oxidation states. However, although halide double perovskites have been crystallographically characterized since the 1930s,[8] with the exception of two $Au^{I}Au^{III}$ perovskites[9] and the recently reported $Cs_4CuSb_2Cl_{12}$,[10] 2D analogs of these materials are lacking. As a result, the physical and electronic consequences of lowering the dimensionality of the inorganic sublattice in halide double perovskites have remained unexplored. Herein, we probe the effects of dimensional confinement on the 3D double perovskite $Cs_2AgBiBr_6$[11] by synthesizing two 2D derivatives: $(BA)_4AgBiBr_8$ (**1**, BA = $CH_3(CH_2)_3NH_3^+$) and $(BA)_2CsAgBiBr_7$ (**2**) (Figure 1A,B). To understand the electronic consequences of dimensional reduction, we use density functional theory (DFT) to calculate the band structures of **1** and **2**. Notably, these calculations reveal a conversion from an indirect to a direct bandgap as the inorganic lattice of $Cs_2AgBiBr_6$ is thinned to a monolayer in **1**. Calculations on a number of model systems allow us to separate the effects of reduced dimensionality from those of the accompanying structural distortions and reveal the electronic-structure evolution as the inorganic layers progressively narrow from the 3D to the 2D lattice. Results of detailed optical

Received: February 7, 2018
Published: March 25, 2018



DOI: 10.1021/jacs.8b01543
J. Am. Chem. Soc. XXXX, XXX, XXX−XXX

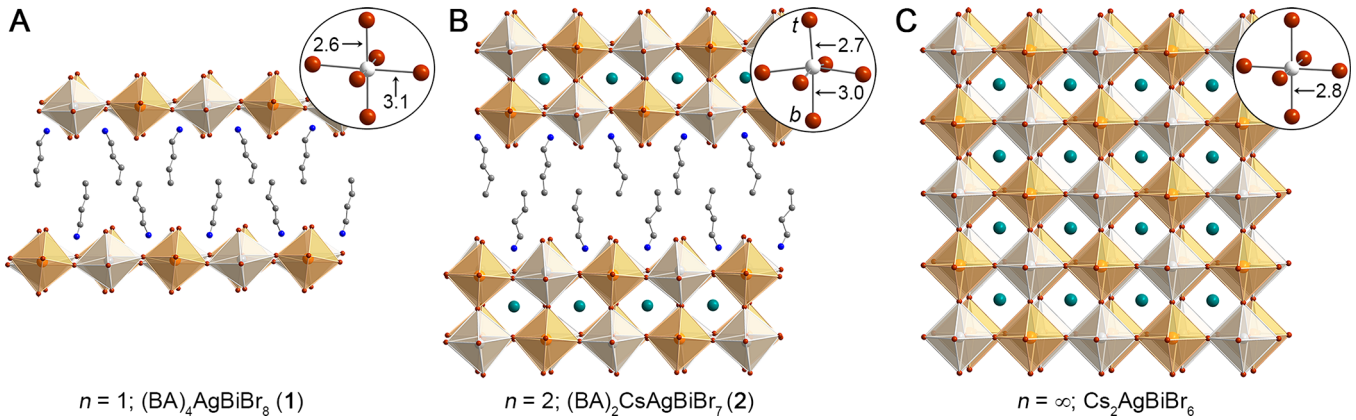


**Figure 1.** Single-crystal X-ray structures (298 K) of the (001) layered double perovskites (A) $(BA)_4AgBiBr_8$ (**1**; BA = $CH_3(CH_2)_3NH_3^+$) and (B) $(BA)_2CsAgBiBr_7$ (**2**), and the 3D double perovskite (C) $Cs_2AgBiBr_6$.[11a] Insets show the Ag coordination sphere with select bond distances in Ångstroms. In the inset for panel B, *t* denotes a terminal bromide and *b* denotes a bridging bromide. Orange, white, turquoise, brown, blue, and gray spheres represent Bi, Ag, Cs, Br, N, and C atoms, respectively. H and disordered atoms omitted for clarity.

characterization of **1** and **2** are consistent with their calculated electronic structures and show striking differences with respect to the optical properties of their well-studied lead-halide analogs.

## RESULTS AND DISCUSSION

**1. Structural Consequences of Dimensional Reduction.** The 3D $A^IB^{II}X_3$ (X = halide) perovskite lattice consists of corner-sharing B−X octahedra, with small cations occupying the A-site cuboctahedral cavities. Placing larger organic cations at the A sites partitions this 3D structure into the $A'^I_2B^{II}X_4$ 2D hybrid perovskite lattice, consisting of single sheets of corner-sharing B−X octahedra ($n = 1$) templated by ordered arrays of organic cations.[12] Layered perovskites with flat inorganic sheets are referred to as (001) perovskites as they resemble a slice cut along the (001) crystallographic plane of the 3D lattice. A mixture of small and large A-site cations affords 2D perovskites with thicker inorganic sheets with the general formula $A'_2A_{n-1}B_nX_{3n+1}$ for (001) perovskites ($\infty > n \geq 1$; A′ = cation that partitions the inorganic sheets, A = cation that is incorporated into the inorganic sheets).[13] The perovskite lattice can be further tuned by varying the elemental composition of the A, B, and X sites.[3a] Substitution at the B site in 3D perovskites can be expanded beyond divalent cations by using a mixture of mono- and trivalent elements, yielding the double-perovskite structure $(A^I_2B^IB'^{III}X_6)$.[8,14] This approach was recently used to synthesize $Cs_2AgBiBr_6$ as a less toxic analog of the lead-halide perovskite solar-cell absorbers.[11] Notably, $Cs_2AgBiBr_6$ showed a slow carrier recombination process[11a] and its bandgap of 1.95 eV could be decreased through dilute impurity alloying.[15] Very recently, dimensional reduction of $Cs_2AgBiBr_6$ through nanostructuring of the bulk material was reported.[16] Seeking to further expand and explore the halide double-perovskite family, we synthesized layered derivatives of $Cs_2AgBiBr_6$.

The layered double perovskite **1** was crystallized from a slowly cooled stoichiometric solution of $BiBr_3$, AgBr, and butylamine in concentrated hydrobromic acid. Single-crystal X-ray diffraction (SC-XRD) of the resulting yellow plate-like crystals revealed a typical $n = 1$ perovskite structure (Figure 1A; with the general formula $A'_2B_{0.5}B'_{0.5}X_4 \times 2$) with an ordered arrangement of $Ag^+$ and $Bi^{3+}$ at the B and B′ sites. Similarly, the $n = 2$ double perovskite **2** was crystallized from a stoichiometric solution of $BiBr_3$, AgBr, and CsBr with an excess of butylamine in concentrated hydrobromic acid (Figure 1B; with the general formula $A'_2ABB'X_7$). Here, the inorganic sheets are two octahedral layers thick with $Ag^+$ and $Bi^{3+}$ ordered in all three dimensions. The $Cs^+$ cations reside in the cavities of the inorganic layers, whereas bilayers of $BA^+$ separate the inorganic slabs.

Unlike in cubic $Cs_2AgBiBr_6$ (Figure 1C),[11a] the inorganic sheets in both **1** and **2** are heavily distorted, particularly at the Ag site. In **1**, the Ag−Br octahedra show a tetragonal distortion with unusually short bonds between Ag and the axial terminal bromides ($Ag-Br_{ax}$ = 2.6156(1) Å), and long bonds between Ag and the bridging equatorial bromides $Ag-Br_{eq}$ = 3.0608(1) Å; Figure 1A). Monovalent Ag adopts a similarly distorted, almost linear structure in a number of compounds including $Ag^IAg^{III}O_2$,[17] and other $d^{10}$ transition metal ions such as $Au^+$, $Cu^+$, and $Hg^{2+}$ share this preference for linear coordination. This tendency has been attributed to mixing of filled transition-metal *n*d orbitals with empty (*n*+1)s orbitals, which stabilizes a linear coordination geometry.[9,18] In **2**, the Ag atoms protrude from either side of the inorganic sheets, sitting 0.38 Å out of the plane defined by the equatorial bridging bromides, and forming a shorter bond with the axial terminal Br (2.6557(1) Å) and a longer bond with the axial bridging Br (3.0148(1) Å) (Figure 1B inset). Similar off-centering of the B-site cation has been observed in some 2D oxide perovskites and attributed to a pseudo-Jahn−Teller effect, where empty metal d orbitals are low enough in energy to mix with filled oxygen p orbitals, stabilizing a distorted geometry.[19] Calculations on model systems replacing the $Ag^+$ in **2** with a series of monocations suggest that the origin of the off-centering in this case may be an electrostatic effect (see Supporting Information).

**2. Electronic Consequences of Dimensional Reduction.** To explore the electronic consequences of reduced dimensionality, we compared DFT band structures of **1** and **2**, calculated with atomic coordinates fixed to those of our 100 K SC-XRD structures, to that of $Cs_2AgBiBr_6$ (also fixed to experiment[20]). The 100 K crystal structures show similar distortions at the Ag site as the 298 K structures (Table S3). In our DFT calculations, we used the PBE exchange-correlation functional and included spin−orbit coupling self-consistently (see Supporting Information for details). In agreement with prior experimental and theoretical results, the band structure of


DOI: 10.1021/jacs.8b01543
J. Am. Chem. Soc. XXXX, XXX, XXX−XXX

the face-centered-cubic lattice in $Cs_2AgBiBr_6$ shows an indirect gap.[11,20] Here, the valence-band maximum (VBM) has Ag d, Bi s, and Br p character at *X* and the conduction-band minimum (CBM) has Ag s, Bi p, and Br p character at *L*.[11b,15,20] The band structure of the monoclinic lattice in **2** (Figure 2A) is very

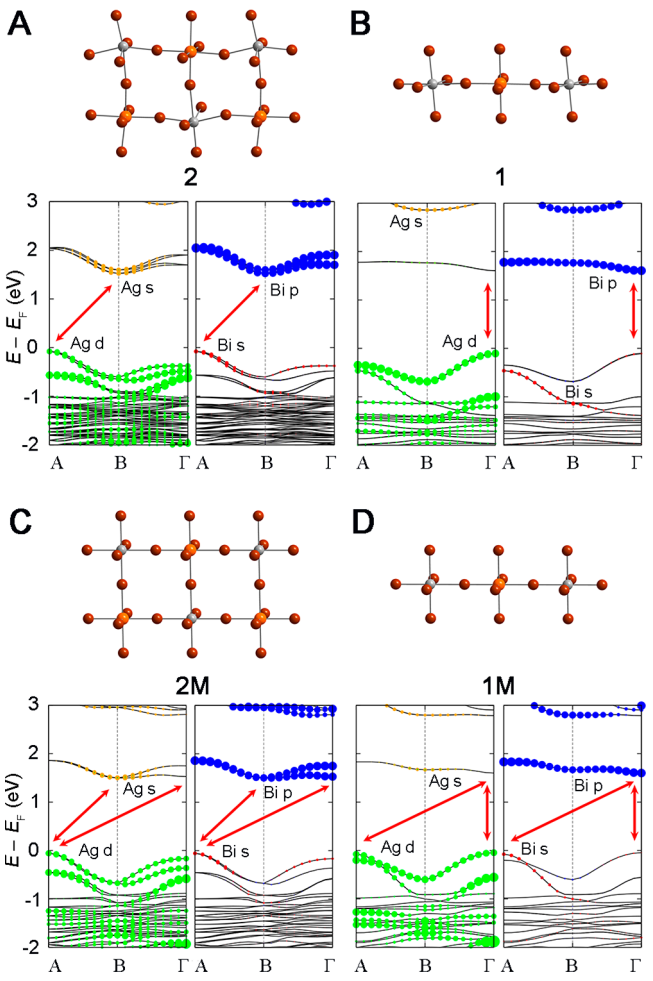


**Figure 2.** Band structures corresponding to the 100 K experimental structures of (A) $(BA)_2CsAgBiBr_7$ (**2**) and (B) $(BA)_4AgBiBr_8$ (**1**) and to the undistorted model structures of (C) $(BA)_2CsAgBiBr_7$ (**2M**), and (D) $(BA)_4AgBiBr_8$ (**1M**). Gray, orange, and brown spheres represent Ag, Bi, and Br atoms, respectively. Note that band structures are shown in duplicate, where the Ag (left panel) and Bi (right panel) states that compose the bands are represented by colored dots. Red arrows show the lowest-energy transitions.

similar, showing the same orbital compositions at the band extrema as for $Cs_2AgBiBr_6$. The VBM of **2** is at the *A* point and its CBM is at the *B* point; the *A* and *B* points of a primitive monoclinic lattice are *k*-space equivalents of the *X* and *L* points, respectively, of a face-centered-cubic lattice (see Supporting Information for the derivation). Thus, the key features of the band structure of **2** derive directly from the band structure of $Cs_2AgBiBr_6$. Furthermore, calculations of simplified model systems (with Cs replacing BA, see Supporting Information for details) for $n = 2$, 3, and 4 structures predict that all materials with $\infty \geq n \geq 2$ have analogous electronic structures, albeit with band dispersion increasing with *n*. As shown in Figure 3, these model systems have indirect bandgaps between the VBM at *A* and the CBM at *B* and a similar orbital composition at the band edges.

In contrast, the band structure of **1** differs greatly from that of $Cs_2AgBiBr_6$. Most notably, we find a direct bandgap at Γ. Unlike in the case of the $\infty \geq n \geq 2$ systems, here, the VBM is composed almost entirely of Ag d and Br p orbitals with very little contribution from Bi s states, while the CBM consists only of Bi and Br p orbitals with all states of Ag s character lying higher in energy. Mixing between Ag and Bi frontier orbitals in both the VB and the CB has been identified as the source of the indirect bandgap in $Cs_2AgBiBr_6$.[11b,15,20,21] Such hybridization is avoided in **1**, which exhibits single-metal-orbital character at its band edges. This transition from an indirect gap in the 3D material to a direct gap in the 2D material is reminiscent of the effects of exfoliation of transition metal dichalcogenides.[2]

Dimensional reduction of $Cs_2AgBiBr_6$ leads to significant distortion of the inorganic lattice. Because both reduced dimensionality and structural distortion could drive the indirect-to-direct bandgap transition, we sought to isolate their effects. We constructed models of the $n = 1$ (**1M**) and 2 (**2M**) derivatives of $Cs_2AgBiBr_6$ using untilted and undistorted metal-halide octahedra, as found in the parent 3D lattice. Band structures of **2M** and **1M** (Figure 2C,D) predict indirect and direct bandgaps, respectively, indicating that dimensional reduction alone is sufficient to explain the emergence of a direct bandgap in the $n = 1$ limit. Nevertheless, clear differences in band dispersion between the model and experimental systems demonstrate how structural distortions in **1** and **2** shape the details of their band structures. For example, **2M** displays indirect bandgaps between the VBM at *A* and the isoenergetic (within 20 meV) CBM at Γ and *B*, but a direct transition at Γ lies only 0.13 eV higher in energy. In contrast, the lowest-energy direct transition in the band structure of **2** lies almost 0.5 eV higher in energy than the lowest-energy indirect transition. This difference results from distortion-induced changes in orbital overlap at the Ag site, which alter the valence band (VB) dispersion. As discussed previously, the Ag sits above the plane of the equatorial bromides, with one long and one short Ag−$Br_{ax}$ bond. This distortion stabilizes the antibonding VBM states of Ag $dz^2$ character at Γ relative to those of Ag $dx^2-y^2$ character at *A*, increasing the energy gap at Γ and leaving the indirect $A \rightarrow B$ transition as the lowest-energy excitation (Figure S12).

The band structure of **1M** displays isoenergetic (within 30 meV) direct (Γ) and indirect (*A* to Γ) bandgaps in contrast to the band diagram of **1**, which has only a direct gap at Γ. This change arises from the axial compression of the Ag−Br octahedra in **1**. The unusually short Ag−$Br_{ax}$ bonds destabilize the antibonding VBM states of Ag $dz^2$ character at Γ, whereas the unusually long Ag−$Br_{eq}$ bonds stabilize those of Ag $dx^2-y^2$ character at A (Figure S12). This lifts the degeneracy of the VBM at Γ and *A*, making the direct transition at Γ the lowest in energy. Because symmetry allows mixing of the Bi s states with the Ag $dx^2-y^2$ states but not with the Ag $dz^2$ states, this distortion also effectively removes all Bi s character from the VBM in **1**. Therefore, although dimensional confinement alone can account for the direct bandgap in the $n = 1$ limit, the accompanying structural distortions energetically separate the direct and indirect transitions and play a significant role in shaping the orbital composition of the band edges.

**3. Optical Characterization.** *Emission.* Luminescence from **1** and **2** is notably different than that of their Pb−Br analogs. Typical $n = 1$ Pb−Br perovskites show narrow, free-excitonic blue photoluminescence (PL) even at room temperature,[22] although lattice distortions have been correlated with


DOI: 10.1021/jacs.8b01543
J. Am. Chem. Soc. XXXX, XXX, XXX−XXX

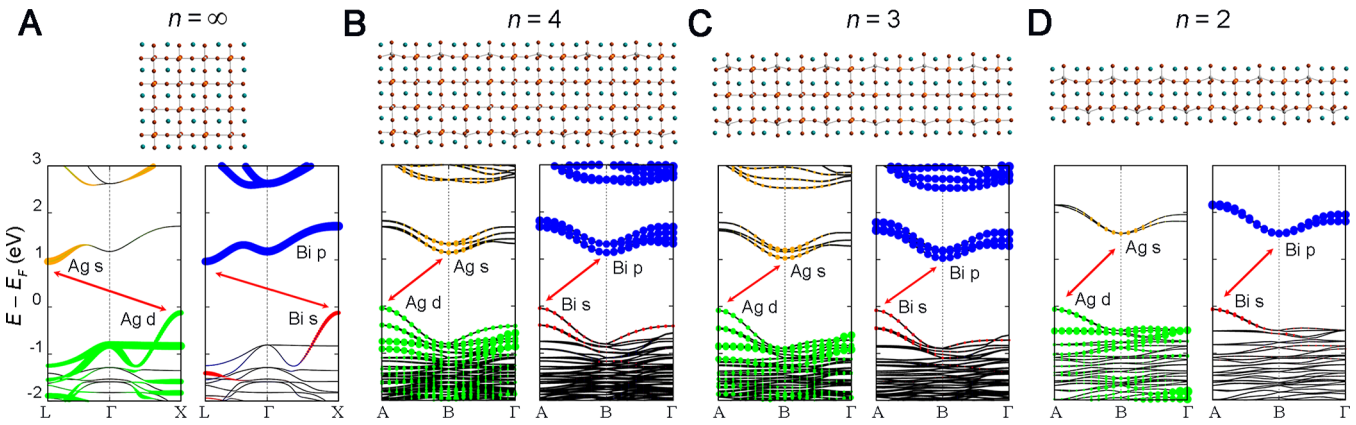


**Figure 3.** Atomic geometries and band structures of $Cs_2AgBiBr_6$ (A) and model $n$ = 4 (B, **4Cs**), $n$ = 3 (C, **3Cs**), and $n$ = 2 (D, **2Cs**) perovskites. Gray, orange, brown, and teal spheres represent Ag, Bi, Br, and Cs atoms, respectively. The dominant metal orbital character of the bands is shown in color. Red arrows indicate the lowest-energy transitions.

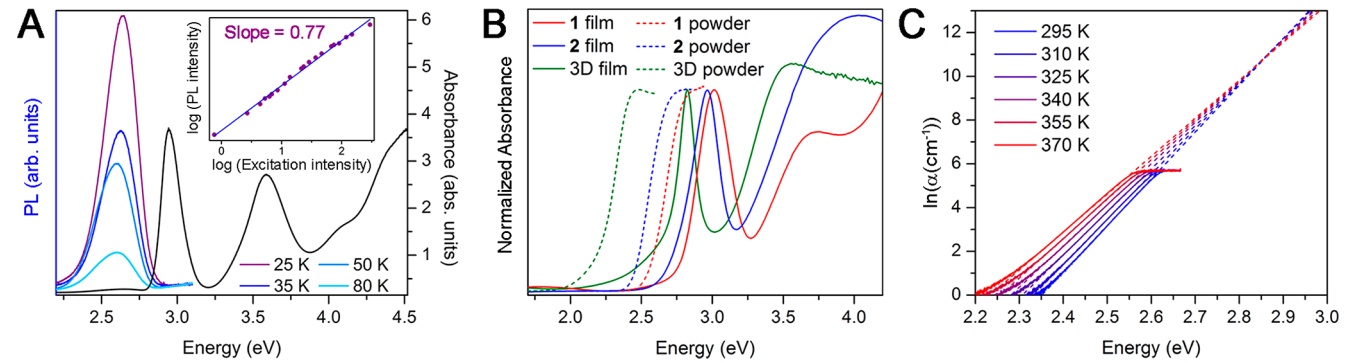


**Figure 4.** (A) Low-temperature photoluminescence (PL) spectra and 7 K absorption spectrum of a film of **1**. Inset: Excitation power ($mW/cm^2$) dependence of the emission intensity. (B) Thin-film transmission spectra (solid lines) and powder diffuse-reflectance spectra (dashed lines) of **1**, **2**, and $Cs_2AgBiBr_6$ (3D). (C) Temperature-dependent transmission spectra of a single crystal of **1**. As expected for an Urbach tail, the absorption coefficient ($\alpha$) shows an exponential dependence on photon energy, and linear fits of the absorption edge over a range of temperatures converge to a single point: 2.85 eV.

broadband white PL.[6b,23] In contrast, films of **1** display weak, slightly broadened PL at 20 K, which quenches rapidly upon warming (Figure 4A). Unlike the excitonic PL from lead-bromide perovskites that displays linear or superlinear behavior,[6,23] the luminescence intensity of films (Figure 4A inset) and powders (Figure S6) of **1** displays a sublinear dependence on incident laser power density, implicating a defect-mediated radiative recombination pathway. PL measurements of powders of **2** also suggest defect-mediated emission (Figure S9). At ca. 20 K, **2** displays three relatively broad luminescence features, two of which strongly resemble the PL from the $n$ = 1 and ∞ members (see Supporting Information and Figure S5). This may result from $n$ = 1 and ∞ domains within the $n$ = 2 perovskite (similar to PL from $n$ > 1 Pb–I perovskite films, where PL from multiple $n$ values is observed)[24] or from similar emissive defects in all these materials.

*Absorption.* The lowest-energy feature in thin-film transmission measurements of **1** is a sharp isolated feature centered at 3.01 eV (Figure 4B). Although reminiscent of the excitonic absorption peaks of 2D lead-halide perovskites,[25] we observe several notable differences. The excitonic absorption peaks of 2D lead halide perovskites are characterized by their extremely narrow line widths (full width at half-maximum (fwhm) of ~100 meV at 298 K[22] and ~50 meV at 5 K (see Supporting Information)) whereas the absorption feature in **1** is three times broader at both room temperature (fwhm of 290 meV) and 9 K (fwhm of 145 meV). Additionally, low-temperature sharpening of the 2D lead-perovskite's excitonic absorption reveals a step-like feature corresponding to the onset of band-edge absorption expected for a 2D density of states (Figure S1).[26] Similar behavior is not observed in **1** at 9 K. We attribute this feature in **1** to a transition involving localized energy levels with a high density of states that gives strong optical absorption over a narrow energy window. This is consistent with the fairly flat valence and conduction bands in the band structure of **1**. Because the VB consists of Ag d and Br p orbitals while the CB consists of Bi p and Br p orbitals, this lowest-energy transition is expected to have considerable Ag to Bi charge-transfer (CT) character. This is in contrast to the analogous lead perovskites, whose bandgap transition involves charge transfer within the same metal: between filled lead 6s and halide p orbitals in the valence band and empty lead 6p states in the conduction band.[27]

The dominant lowest-energy feature in the thin-film transmission spectra of **2** and $Cs_2AgBiBr_6$ is also a similar sharp feature (located at 2.96 eV in **2** and 2.82 eV in $Cs_2AgBiBr_6$[16]), showing only a slight red-shift with increasing $n$ (Figure 4B). This strong absorption feature, which is almost energetically invariant with $n$ ($\Delta E$ = 50 meV for $n$ = 1 and 2), explains the color of the layered double perovskites. Polycrystalline powders of **1** and **2** are both bright yellow,


DOI: 10.1021/jacs.8b01543
J. Am. Chem. Soc. XXXX, XXX, XXX–XXX

whereas their $n$ = 1 and 2 Pb−Br analogs are colorless and pale yellow (Figure 5), respectively, reflecting the change in

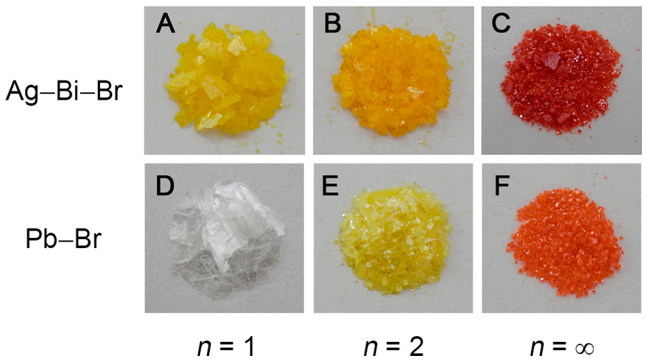


**Figure 5.** Small crystals of **1** (A), **2** (B), and $Cs_2AgBiBr_6$ (C) shown with the analogous lead-bromide perovskites, $(BA)_2PbBr_4$ (D), $(BA)_2(MA)Pb_2Br_7$ (E), and $(MA)PbBr_3$ (F) (MA = $CH_3NH_3^+$).

excitonic absorption energy ($E_{ex}$) with $n$ ($\Delta E_{ex}$ = 210 meV for $n$ = 1 $(BA)_2PbBr_4$[23] and $n$ = 2 $(BA)_2(MA)Pb_2Br_7$[28]). The similarity of these sharp absorption features in **2** and $Cs_2AgBiBr_6$ to that in **1** suggests that they arise from a related transition and thus, possess Ag→Bi CT character. In **1**, this CT transition occurs at the bandgap, which has single-metal character at the band edges. However, in order to find a transition between orbitals of single-metal character (with no mixing between Ag and Bi states) in **2** and $Cs_2AgBiBr_6$, we must move away from the band extrema and consider higher-energy transitions, either deeper in the bands or at a different $k$-point. Thus, in **2** and $Cs_2AgBiBr_6$, the strong CT transition is not expected to be the lowest-energy feature in the absorption spectrum.

In $Cs_2AgBiBr_6$, the CT absorption lies above both the indirect (1.95 eV) and direct band edges. Nevertheless, in thin films, the intense CT peak dwarfs the absorption at the indirect and direct edges, likely due to the high density of states of the levels involved. In fact, the absorption onset at the bandgap of $Cs_2AgBiBr_6$ is essentially unobservable in films that are 130 nm thick, consistent with a small absorption coefficient ($<10^4$ $cm^{-1}$) for this indirect transition. Similarly, the calculated lowest-energy excitation in **2** is an indirect transition, which should yield absorption that is too weak to observe clearly in thin films. Though the small absorption coefficient of indirect transitions makes these excitations difficult to observe in thin-film measurements, we expect to see them in thicker samples. Indeed, the absorption onset of $Cs_2AgBiBr_6$ is much more evident in powders[11] (Figure 4B). Similarly, powders of **2** show an absorption onset of 2.4 eV, which is 0.3 eV lower than the apparent onset in the film, consistent with its calculated indirect gap (Figure 4B).

Although electronic structure calculations show a direct gap transition in **1**, powders of **1** also show a lower-energy absorption onset than the corresponding films, similar to **2** and $Cs_2AgBiBr_6$. However, the shallow absorption onset in **1** may have a different origin. Temperature-dependent transmission measurements on a large (3 mm × 5 mm × 0.08 mm) single crystal of **1** show that the absorption edge varies exponentially with photon energy over a wide range of temperatures (8−370 K). When plotted on a logarithmic scale, linear fits of the absorption coefficient as a function of photon energy between 295 and 370 K converge to a single point (Figure 4C), in accordance with the Urbach rule.[29] The $x$-value of this point (2.85 eV) gives a rough estimate of the bandgap,[30] which is in reasonable agreement with the absorption onset of a thin film (2.77 eV, see Supporting Information for details). At lower temperatures, the linear fits deviate from a single convergence point. We attribute this deviation to a phase transition that occurs just below room temperature (also evidenced by SC-XRD, see Supporting Information) as well as deviations from ideal Urbach behavior below the Debye temperature.[29] This suggests that the weak low-energy absorption observed in powder samples arises from the interaction of excitations with lattice disorder (i.e., an Urbach tail) rather than from an indirect bandgap. Our inability to grow suitable crystals precluded a similar analysis of **2**.

## CONCLUSIONS

We show the structural and electronic consequences of dimensional reduction in a new family of halide double perovskites. The 3D double perovskite $Cs_2AgBiBr_6$ displays an indirect bandgap with contributions from both Ag and Bi orbitals at the band edges. This band structure is retained until the thickness of the inorganic sublattice is reduced to a monolayer in **1**. Intriguingly, calculations predict a direct bandgap in **1**, and, here, we see only single-metal character at the band edges. Calculations on model systems reveal that this indirect-to-direct bandgap transition is driven primarily by dimensional confinement, although the accompanying structural distortions further separate the lowest-energy direct and indirect gaps in **1** and **2**. Perovskites **1**, **2**, and $Cs_2AgBiBr_6$ show a strong absorption feature at similar energies, which we assign to Ag-to-Bi charge-transfer. The energetic invariance of this feature between the $n$ = 1 and 2 perovskites is responsible for the similar yellow color of these solids. Our optical data support indirect bandgaps for **2** and $Cs_2AgBiBr_6$, with weak absorption onsets evident in comparisons of thin-film and powder absorption measurements. An Urbach-tail analysis of a single crystal of **1** gives values for its optical bandgap that agree with those obtained from thin-film measurements. This analysis suggests that the weak absorption onset in **1** is due to the interaction of excitations with lattice disorder/defects rather than an indirect bandgap. Although not conclusive evidence, this supports the prediction of a direct bandgap in this material and is consistent with its defect-mediated photoluminescence. We are continuing to study the impact of dimensional reduction on the electronic structure and excitonic properties of this family of double perovskites.

Double perovskites considerably increase the compositional diversity of halide perovskites, and their expansion to lower-dimensional hybrids further widens their accessible electronic platforms. The very different photophysical properties of 2D double perovskites, compared to their single-metal analogs, motivate continued investigations of this unexplored class of mixed-metal hybrids. In particular, dimensional reduction of the inorganic sublattice through the inclusion of organic molecules should be further studied as a strategy for attaining direct-gap hybrids from indirect-gap inorganic solids.

## ASSOCIATED CONTENT

### Supporting Information

The Supporting Information is available free of charge on the ACS Publications website at DOI: 10.1021/jacs.8b01543.



DOI: 10.1021/jacs.8b01543
J. Am. Chem. Soc. XXXX, XXX, XXX−XXX

Experimental details, crystallographic data, and spectra (PDF)
Data for $(BA)_4AgBiBr_8$ (1), 100 K (CIF)
Data for $(BA)_4AgBiBr_8$ (1), 298 K (CIF)
Data for $(BA)_2CsAgBiBr_7$ (2), 100 K (CIF)
Data for $(BA)_2CsAgBiBr_7$ (2), 298 K (CIF)
Data for $Cs_4AgBiBr_8$ (1Cs) (CIF)
Data for $Cs_3AgBiBr_7$ (2Cs) (CIF)
Data for $Cs_8Ag_3Bi_3Br_{20}$ (3Cs) (CIF)
Data for $Cs_5Ag_2Bi_2Br_{13}$ (4Cs) (CIF)
Data for $(BA)_4AgBiBr_8$ (1R) (CIF)
Data for $(BA)_2CsAgBiBr_7$ (2R) (CIF)

### Accession Codes

The CIFs for **1** (100 K), **1** (298 K), **2** (100 K), and **2** (298 K) have been deposited in the Cambridge Crystallographic Data Centre under deposition numbers 1814797−1814800, respectively.

## AUTHOR INFORMATION


### Corresponding Authors

*hemamala@stanford.edu
*jbneaton@lbl.gov

### ORCID

Matthew D. Smith: 0000-0002-4197-5176
Hemamala I. Karunadasa: 0000-0003-4949-8068


### Notes

The authors declare no competing financial interest.

## ACKNOWLEDGMENTS

This research was funded by the SLAC National Laboratory and the National Science Foundation (NSF) CAREER award (DMR-1351538). SC-XRD studies were performed at beamline 11.3.1 at the Advanced Light Source (ALS) at the Lawrence Berkeley National Laboratory. Part of this work was performed at the Stanford Nano Shared Facilities, supported by the NSF (award ECCS-1542152). B.A.C. is supported by an NSF graduate fellowship (DGE-114747) and M.D.S. is supported by graduate fellowships from the NSF (DGE-114747) and the Stanford Center for Molecular Design (CMAD). Work by J.B.N. and L.L. was funded by the U.S. Department of Energy, Office of Science, Office of Basic Energy Sciences (DOE, BES), Materials Sciences and Engineering Division (DE-AC02-05CH11231). L.L. acknowledges partial support by the Feodor-Lynen program of the Alexander von Humboldt foundation. Work at the Molecular Foundry and the ALS was supported by the DOE, BES (DE-AC02-05CH11231). We thank A. H. Slavney for helpful discussions, Dr. S. Teat for assistance with crystallography, and Profs. M. D. McGehee and E. I. Solomon for access to equipment.

## REFERENCES


(1) Tulsky, E. G.; Long, J. R. *Chem. Mater.* **2001**, *13*, 1149.
(2) (a) Splendiani, A.; Sun, L.; Zhang, Y.; Li, T.; Kim, J.; Chim, C.-Y.; Galli, G.; Wang, F. *Nano Lett.* **2010**, *10*, 1271. (b) Mak, K. F.; Lee, C.; Hone, J.; Shan, J.; Heinz, T. F. *Phys. Rev. Lett.* **2010**, *105*, 136805.
(3) (a) Saparov, B.; Mitzi, D. B. *Chem. Rev.* **2016**, *116*, 4558. (b) Pedesseau, L.; Sapori, D.; Traore, B.; Robles, R.; Fang, H.-H.; Loi, M. A.; Tsai, H.; Nie, W.; Blancon, J.-C.; Neukirch, A.; Tretiak, S.; Mohite, A. D.; Katan, C.; Even, J.; Kepenekian, M. *ACS Nano* **2016**, *10*, 9776.
(4) (a) Kojima, A.; Teshima, K.; Shirai, Y.; Miyasaka, T. *J. Am. Chem. Soc.* **2009**, *131*, 6050. (b) Green, M. A.; Ho-Baillie, A.; Snaith, H. J. *Nat. Photonics* **2014**, *8*, 506.
(5) (a) Era, M.; Morimoto, S.; Tsutsui, T.; Saito, S. *Appl. Phys. Lett.* **1994**, *65*, 676. (b) Byun, J.; Cho, H.; Wolf, C.; Jang, M.; Sadhanala, A.; Friend, R. H.; Yang, H.; Lee, T.-W. *Adv. Mater.* **2016**, *28*, 7515. (c) Yuan, M.; Quan, L. N.; Comin, R.; Walters, G.; Sabatini, R.; Voznyy, O.; Hoogland, S.; Zhao, Y.; Beauregard, E. M.; Kanjanaboos, P.; Lu, Z.; Kim, D. H.; Sargent, E. H. *Nat. Nanotechnol.* **2016**, *11*, 872.
(6) (a) Gauthron, K.; Lauret, J.-S.; Doyennette, L.; Lanty, G.; Al Choueiry, A.; Zhang, S. J.; Brehier, A.; Largeau, L.; Mauguin, O.; Bloch, J.; Deleporte, E. *Opt. Express* **2010**, *18*, 5912. (b) Dohner, E. R.; Jaffe, A.; Bradshaw, L. R.; Karunadasa, H. I. *J. Am. Chem. Soc.* **2014**, *136*, 13154.
(7) Mitzi, D. B. *Inorg. Chem.* **2000**, *39*, 6107.
(8) Elliott, N.; Pauling, L. *J. Am. Chem. Soc.* **1938**, *60*, 1846.
(9) Castro-Castro, L. M.; Guloy, A. M. *Angew. Chem., Int. Ed.* **2003**, *42*, 2771.
(10) Vargas, B.; Ramos, E.; Pérez-Gutiérrez, E.; Alonso, J. C.; Solis-Ibarra, D. *J. Am. Chem. Soc.* **2017**, *139*, 9116.
(11) (a) Slavney, A. H.; Hu, T.; Lindenberg, A. M.; Karunadasa, H. I. *J. Am. Chem. Soc.* **2016**, *138*, 2138. (b) McClure, E. T.; Ball, M. R.; Windl, W.; Woodward, P. M. *Chem. Mater.* **2016**, *28*, 1348.
(12) Mitzi, D. B. *J. Chem. Soc., Dalton Trans.* **2001**, 1.
(13) Calabrese, J.; Jones, N. L.; Harlow, R. L.; Herron, N.; Thorn, D. L.; Wang, Y. *J. Am. Chem. Soc.* **1991**, *113*, 2328.
(14) (a) Cross, W.; Hillebrand, W. F. Contributions to the Mineralogy of the Rocky Mountains. In *Bulletin of the United States Geological Survey No. 20*; Government Printing Office: Washington D.C., 1885. (b) Frondel, C. *Am. Mineral.* **1948**, *33*, 84. (c) Wells, H. L. *Am. J. Sci.* **1922**, *s5-3*, 315.
(15) Slavney, A. H.; Leppert, L.; Bartesaghi, D.; Gold-Parker, A.; Toney, M. F.; Savenije, T. J.; Neaton, J. B.; Karunadasa, H. I. *J. Am. Chem. Soc.* **2017**, *139*, 5015.
(16) Creutz, S. E.; Crites, E. N.; De Siena, M. C.; Gamelin, D. R. *Nano Lett.* **2018**, *18*, 1118.
(17) McMillan, J. A. *J. Inorg. Nucl. Chem.* **1960**, *13*, 28.
(18) (a) Orgel, L. E. *J. Chem. Soc.* **1958**, 4186. (b) Pearson, R. G. *J. Am. Chem. Soc.* **1969**, *91*, 4947.
(19) (a) Bhuvanesh, N. S. P.; Gopalakrishnan, J. *J. Mater. Chem.* **1997**, *7*, 2297. (b) Kodenkandath, T. A.; Wiley, J. B. *Mater. Res. Bull.* **2000**, *35*, 1737. (c) Bersuker, I. B. *Chem. Rev.* **2013**, *113*, 1351.
(20) Filip, M. R.; Hillman, S.; Haghighirad, A. A.; Snaith, H. J.; Giustino, F. *J. Phys. Chem. Lett.* **2016**, *7*, 2579.
(21) Savory, C. N.; Walsh, A.; Scanlon, D. O. *ACS Energy Lett.* **2016**, *1*, 949.
(22) Kitazawa, N. *Mater. Sci. Eng., B* **1997**, *49*, 233.
(23) Smith, M. D.; Jaffe, A.; Dohner, E. R.; Lindenberg, A. M.; Karunadasa, H. I. *Chem. Sci.* **2017**, *8*, 4497.
(24) Smith, I. C.; Hoke, E. T.; Solis-Ibarra, D.; McGehee, M. D.; Karunadasa, H. I. *Angew. Chem., Int. Ed.* **2014**, *53*, 11232.
(25) (a) Ishihara, T.; Takahashi, J.; Goto, T. *Solid State Commun.* **1989**, *69*, 933. (b) Ishihara, T.; Takahashi, J.; Goto, T. *Phys. Rev. B: Condens. Matter Mater. Phys.* **1990**, *42*, 11099.
(26) Hong, X.; Ishihara, T.; Nurmikko, A. V. *Solid State Commun.* **1992**, *84*, 657.
(27) Ishihara, T.; Hirasawa, M.; Goto, T. *Jpn. J. Appl. Phys.* **1995**, *34*, 71.
(28) Chen, J.; Wang, Y.; Gan, L.; He, Y.; Li, H.; Zhai, T. *Angew. Chem., Int. Ed.* **2017**, *56*, 14893.
(29) Kurik, M. V. *Phys. Stat. Sol. (A)* **1971**, *8*, 9.
(30) Tang, H.; Lévy, F.; Berger, H.; Schmid, P. E. *Phys. Rev. B: Condens. Matter Mater. Phys.* **1995**, *52*, 7771.



DOI: 10.1021/jacs.8b01543
J. Am. Chem. Soc. XXXX, XXX, XXX−XXX